Nanoscale

PAPER

View Article Online
View Journal | View Issue

Cite this: *Nanoscale*, 2018, **10**, 20414

In situ grown nickel selenide on graphene nanohybrid electrodes for high energy density asymmetric supercapacitors†

Balakrishnan Kirubasankar, [a,b] Vignesh Murugadoss, [a,c,d] Jing Lin,*[b] Tao Ding,*[c] Mengyao Dong,[d,e] Hu Liu, [e] Jiaoxia Zhang,[d,f] Tingxi Li,*[g] Ning Wang,[h] Zhanhu Guo *[d] and Subramania Angaiah *[a]

Nickel selenide (NiSe) nanoparticles uniformly supported on graphene nanosheets (G) to form NiSe–G nanohybrids were prepared by an *in situ* hydrothermal process. The uniform distribution of NiSe on graphene bestowed the NiSe–G nanohybrid with faster charge transport and diffusion along with abundant accessible electrochemical active sites. The synergistic effect between NiSe nanoparticles and graphene nanosheets for supercapacitor applications was systematically investigated for the first time. The free-standing NiSe–G nanohybrid electrode exhibited better electrochemical performance with a high specific capacitance of 1280 F g^{-1} at a current density of 1 A g^{-1} and a capacitance retention of 98% after 2500 cycles relative to that of NiSe nanoparticles. Furthermore, an asymmetric supercapacitor device assembled using the NiSe–G nanohybrid as the positive electrode, activated carbon as the negative electrode and an electrospun PVdF membrane containing 6 M KOH as both the separator and the electrolyte delivered a high energy density of 50.1 W h kg^{-1} and a power density of 816 W kg^{-1} at an extended operating voltage of 1.6 V. Thus, the NiSe–G nanohybrid can be used as a potential electrode material for high-performance supercapacitors.

Received 6th August 2018,
Accepted 1st October 2018

DOI: 10.1039/c8nr06345a

rsc.li/nanoscale

1. Introduction

Supercapacitors or electrochemical capacitors have been widely investigated as promising energy storage systems because of their high power density, expeditious charge–discharge, long cycle life and environmental friendliness.[1–4] Based on the charge storage mechanisms, they are classified as electrical double layer capacitors (EDLCs) and pseudo-capacitors. The pseudo-capacitors possess higher specific capacitance than EDLCs because of the faradaic charge storage mechanisms.[5] However, their energy density is lower than that of rechargeable batteries, which hinders their practical applications. Hence, there is an intense demand to increase the energy density of supercapacitors without conceding their power density. The energy density of supercapacitors can be improved by increasing the capacitance of the electrode material (C) or its operating voltage window (V) or both since the energy stored is proportional to $C{\cdot}V^2$.[6]

Asymmetric supercapacitors (ASCs) are an effective tool to increase the energy density and cell voltage. ASCs consist of a faradaic positive electrode as the energy source and an EDLC-type negative electrode as the power source, offering the advantages of both a supercapacitor (power density, rate, and cycle life) and a battery (energy density). In addition, different electrode materials in one system expand the operating voltage. To obtain excellent supercapacitor performance, the electrode material should possess better electrochemical redox reactions, superior electrical conductivity, high chemical stability and a shorter diffusion path for both electrons and electrolyte ions.[7–12] Activated carbon and graphene with high specific

[a]*Electro-Materials Research Laboratory, Centre for Nanoscience and Technology, Pondicherry University, Puducherry - 605014, India. E-mail: a.subramania@gmail.com*
[b]*School of Chemistry and Chemical Engineering, Guangzhou University, Guangzhou 510006, China. E-mail: linjing@gzhu.edu.cn*
[c]*College of Chemistry and Chemical Engineering, Henan University, Kaifeng 475004, China. E-mail: dingtao@henu.edu.cn*
[d]*Integrated Composites Laboratory (ICL), Department of Chemical and Biomolecular Engineering, University of Tennessee, 322, Dougherty Engineering Bldg., Knoxville, USA. E-mail: zguo10@utk.edu*
[e]*Key Laboratory of Materials Processing and Mold (Zhengzhou University), Ministry of Education; National Engineering Research Center for Advanced Polymer Processing Technology, Zhengzhou University, Zhengzhou, 450002, China*
[f]*School of Materials Science and Engineering, Jiangsu University of Science and Technology, Zhenjiang 212003, China*
[g]*College of Materials Science and Engineering, Shandong University of Science and Technology, Qingdao 266590, China. E-mail: litx@sdust.edu.cn*
[h]*State Key Laboratory of Marine Resource Utilization in South China Sea, Hainan University, Haikou 570228, P.R. China*

†Electronic supplementary information (ESI) available. See DOI: 10.1039/c8nr06345a

surface area, better chemical stability, and good electrical conductivity have commonly been used as negative electrodes and others.[13] Further research effort has also been made to explore efficient faradaic positive electrode materials with high capacitance and long cycle life. Inorganic nanoparticles grown on graphene were demonstrated to be viable electrode materials for asymmetric supercapacitors.[14–16] Graphene can be a perfect substrate for the growth of functional nanomaterials for electrochemical energy devices because it offers high specific surface area, high electrical conductivity, and good mechanical flexibility and is electrochemically active.[17–19] Transition metal oxides, sulfides, and selenides have been explored as high-performance supercapacitor materials because of their rich valence state for a reversible faradaic reaction, abundance, low cost and environmental friendliness.[20–24] For transition metal selenides, a sandwich structure is always observed, with a metal atom at the center of two selenide layers.[25] Due to its relatively lower electronegativity than that of oxide and sulfide ions, the selenide ions could create more flexible structures and thereby can prevent the disintegration of the structure by elongation between the layers during charge–discharge cycles. This behavior can also be attributed to easier charge transportation, thus favoring the use of transition metal selenides as a superior electrode material for supercapacitors.[26,27] Recently, CoSe–G nanohybrids demonstrated better supercapacitive performance than CoSe nanoparticles while serving as a positive electrode for supercapacitors.[28]

Compared with polymers or their corresponding metals, metal chalcogenides such as nickel selenide (NiSe) are attracting increasing attention due to high electrocatalytic activity, which makes them a promising material for various applications such as oxygen and hydrogen evolution reactions, dye sensitized solar cells, optoelectronic devices, wastewater treatment, and electrochemical energy conversion/storage.[29–36] Recently, NiSe has been reported to be an efficient electrode material for supercapacitor applications.[37,38] However, there is no report on the nickel selenide/graphene (NiSe–G) nanohybrid as a positive electrode material for asymmetric supercapacitors.

Herein, we report nickel selenide nanoparticles grown on graphene nanosheets by a one step hydrothermal method to form synergistic effects of highly conductive graphene substrates and electrochemically active nickel selenide sites. Their structure, morphology, and composition were confirmed by X-ray diffraction (XRD), Raman spectroscopy, field emission scanning electron microscopy (FE-SEM), transmission electron microscopy (TEM) and X-ray photoelectron spectroscopy (XPS) studies. The feasibility to use them as an efficient positive electrode material was tested in the asymmetric supercapacitors. The effects of graphene on their electrochemical and supercapacitive behaviors were also studied. The electrochemical activities of the prepared NiSe and NiSe–G nanohybrids were studied using electrochemical impedance, cyclic voltammetry (CV) and galvanostatic charge–discharge studies. Asymmetric supercapacitors (ASC) were fabricated using NiSe–G nanohybrids as a positive electrode and activated carbon (AC) as a negative electrode and 6 M KOH soaked in an electrospun polyvinylidene fluoride (PVDF) polymer membrane as an electrolyte as well as a separator. The energy storage performance of these electrodes was evaluated and compared with the recently reported transition metal chalcogenide based electrodes for ASC.

2. Experimental section

2.1 Materials used

Nickel chloride hexahydrate ($NiCl_2{\cdot}6H_2O$, 98% pure), sodium nitrate ($NaNO_3$, 99% pure), hydrazine hydrate ($N_2H_4{\cdot}H_2O$, 99–100% pure), and *N*-methyl-2-pyrrolidinone (NMP, 99% pure) were purchased from Merck. Selenium powder (Se, >99.5% trace metal basis) and polyvinylidene fluoride (PVdF, molecular weight 530 000) were obtained from Sigma-Aldrich. All chemical reagents were of analytical grade and were used as received.

2.2 Preparation of NiSe–G nanohybrids

The NiSe–G nanohybrids were prepared by a simple hydrothermal method. Briefly, 0.0691 g nickel chloride ($NiCl_2$) and 0.0229 g selenium (Se) powders were taken in a 1 : 1 mole ratio and then dissolved in 50 mL of deionized water. Into this, the required quantity of graphene oxide (0.02 g) prepared by a modified Hummers' method[39] was dispersed by ultrasonication. To this, hydrazine (10 mL) was then added drop by drop with constant stirring to act as a reduction agent to increase the graphitization nature of graphene as well as the reduction of Ni^{2+} to form nickel selenide nanoparticles onto graphene. This mixture was transferred into a Teflon-lined stainless steel autoclave and kept at 120 °C for 12 h. After being cooled down to room temperature, the obtained precipitate was washed several times with distilled water and kept inside a vacuum oven at 50 °C for 12 h to obtain the NiSe–G nanohybrid with a mass ratio of 1.0 : 0.5. Pure NiSe nanoparticles were also prepared under the same reaction conditions without the addition of graphene oxide.

2.3 Physical characterization

The morphology and nanostructures of the prepared NiSe nanoparticles and NiSe–G nanohybrids were observed by using field emission scanning electron microscopy (JSM, JEOL 7600F) and high-resolution transmission electron microscopy (Philips, model: CM 200). X-ray photoelectron spectroscopic (XPS) data were acquired using a Kratos AXIS Ultra DLD (Kratos Analytical Ltd) with an X-ray source of mono Al-Kα (1486.71 eV, 5 mA) and an operating power of 75 W. Unless mentioned otherwise, the data were acquired at an angle of 90° between the substrate and the detector, with a step size of 1 eV and a dwell time of 100 ms. The fitting and deconvolution of peaks were carried out using the XPSPEAK 4.1 software. The peaks were referenced with respect to the C 1s peak at 284.6 eV. Information about the phase and crystallinity was obtained by the X-ray diffraction technique (Rigaku, Ultima IV) with nickel-filtered Cu-Kα radiation in the range of 20 to 80° with an increment of 0.05°. The Raman spectra were recorded using

a confocal micro-Raman spectrometer (Renishaw RM 2000) under a 20 mW Innova Ar^+ ion laser at 514 nm.

2.4 Electrochemical characterization and fabrication of ASC devices

The supercapacitive properties of the prepared NiSe nanoparticle and NiSe–G nanohybrid electrodes were measured in a three-electrode cell configuration. The NiSe and NiSe–G electrodes were used as working electrodes. A saturated calomel electrode (SCE), a platinum electrode and a 6 M KOH solution were used as the reference electrode, the counter electrode, and the electrolyte, respectively. The working electrode was prepared by mixing 80 wt% of the prepared electroactive material (NiSe/NiSe–G), 10 wt% of black pearl carbon (activated carbon) and 10 wt% of poly(vinylidene fluoride) in *N*-methyl-2-pyrrolidone to form a homogeneous slurry. This was coated on the stainless steel (SS) substrate with a geometric surface area of 1 cm^2 and then dried at 70 °C for 5 h in a vacuum oven. All the electrochemical performance measurements were carried out using an electrochemical workstation (Biologic Model; VSP, France). Cyclic voltammetry curves were recorded in the potential window of −0.2 to +0.4 V at various scan rates such as 5, 10, 25, 50 and 100 mV s^{-1}. Galvanostatic charge–discharge curves were recorded at various current densities such as 1, 3, 5, 7 and 10 A g^{-1} in the potential range of −0.2 to +0.4 V. Electrochemical impedance measurements were recorded in the frequency range of 0.01 Hz–100 kHz at the open circuit potential with an AC amplitude of 5 mV.

The ASC devices were fabricated using NiSe–G nanohybrid as the cathode and activated carbon as the anode and the electrospun PVDF polymer electrolyte membrane was prepared as per the procedure reported elsewhere[40] and soaked in 6 M KOH as the electrolyte as well as the separator.

From the charge–discharge curves, the specific capacitance (C_{sp}) of the working electrode and the ASC device was calculated using eqn (1):[41]

$$C_{sp} = \frac{i \times \Delta t}{\Delta V \times m} \quad (1)$$

where ΔV is the potential drop during discharge (V), Δt is the discharge time (s) and m is the mass of the active electrode material (g). To obtain the charge balance between the two electrodes, an optimum mass balance of the positive and negative electrodes was calculated using eqn (2):

$$\frac{m_+}{m_-} = \frac{C_- \times \Delta V_-}{C_+ \times \Delta V_-} \quad (2)$$

where C_+/C_- represents the specific capacitance of the positive and negative electrodes, m is the mass of the active material, and $\Delta V_+/\Delta V_-$ is the potential window of the positive and negative electrodes in the three-electrode system.

Electrochemical studies such as cyclic voltammetry and galvanostatic charge–discharge studies were performed for the assembled ASC device. From the charge–discharge curves, the energy density (E) and power density (P) of the ASC device were calculated using eqn (3) and (4):

$$E = \frac{C_{sp} \times V^2}{2} \quad (3)$$

$$P = \frac{E}{t} \quad (4)$$

where C_{sp} is the specific capacitance of the ASC device (F g^{-1}), V is the potential window of the ASC device, and Δt is the discharge time.

3. Results and discussion

Fig. 1 shows FE-SEM images of NiSe nanoparticles, graphene oxide, and NiSe–G nanohybrids, respectively. Pure NiSe nanoparticles aggregate to form large agglomerations (Fig. 1a). Fig. 1b shows that pure graphene oxide possesses a two-dimensional thin wrinkle sheet-like structure. Fig. 1c shows uniform-size NiSe nanoparticles uniformly distributed onto graphene nanosheets and some were wrapped by graphene nanosheets. The functional groups in graphene oxide such as –OH and –COOH could serve as active sites for Ni^{2+} adsorption, which led to the homogeneous distribution of NiSe nanoparticles on the surface of graphene nanosheets.[42] In NiSe–G nanohybrids, the incorporated graphene nanosheets are observed to prevent the aggregation of NiSe nanoparticles.

Fig. S1† shows the energy dispersive X-ray analysis (EDX) of NiSe nanoparticles and NiSe–G nanohybrids, respectively. The

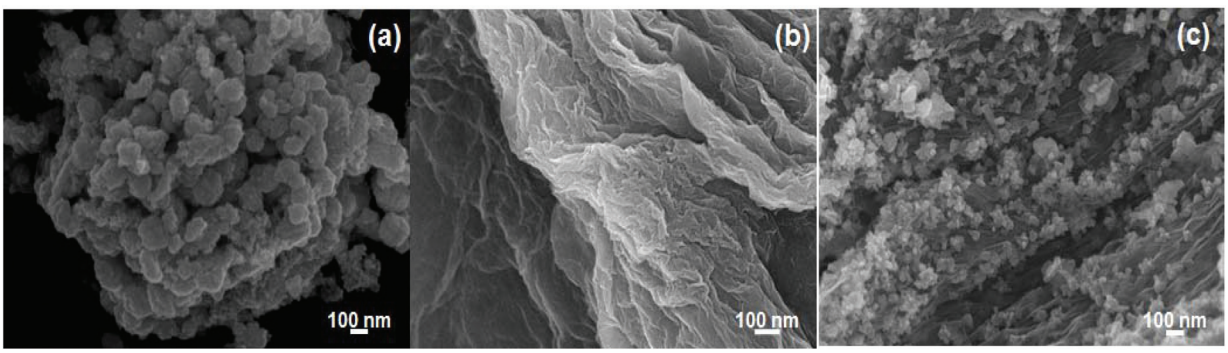

Fig. 1 FE-SEM images of (a) NiSe nanoparticles, (b) graphene oxide and (c) NiSe–G nanohybrids.

NiSe samples displayed the presence of Ni and Se, whereas in the NiSe–G nanohybrid samples displayed the presence of C, Ni and Se species clearly in EDX spectra. The atomic percentages of Ni and Se were found to be 46.01 and 53.99, respectively, and hence the corresponding stoichiometric ratio is confirmed to be $Ni_{0.85}Se$.

Fig. 2 shows a HRTEM image of the NiSe nanoparticles and NiSe–G nanohybrids. Fig. 2a shows that the synthesized NiSe nanoparticles are spherical in shape with an average mean diameter of 23 nm and agglomerate with each other. It is observed that the homogeneously distributed NiSe nanoparticles have better contact with graphene nanosheets due to the presence of wrinkles (Fig. 2c). The SAED diffraction rings of the NiSe nanoparticles (Fig. 2b) and NiSe–G nanohybrids (Fig. 2d) can be indexed to the (101), (103), (201), (211) and (212) planes of NiSe (space group: *P*63/*mmc*, JCPDS no. 18-0888), indicating the polycrystalline nature of NiSe.

Furthermore, elemental mapping using TEM was carried out to elucidate the distribution of chemical elements in the NiSe–G nanohybrid. The elemental distribution image of the NiSe–G nanohybrid (Fig. 3) shows a uniform distribution of nickel (Ni) and selenium (Se) elements in the investigated region (Fig. S2†), indicating the formation of nickel selenide nanoparticles and thereby validating that the nickel selenide nanoparticles are homogeneously dispersed on the graphene nanosheets as observed from FESEM and HRTEM studies. Also, no other impurity elements are observed.

XPS was employed to explore the nature of chemical bonding and chemical state of NiSe–G nanohybrids. The XPS spectrum of NiSe–G nanohybrids (Fig. 4a) clearly shows the obvious peaks of C 1s, O 1s, Ni 2p, and Se 3d originating from graphene and NiSe in the NiSe–G hybrid. The presence of the O 1s peak was due to the unavoidable adsorption of oxygen on the surface of hybrids from the environment. The carbon peak (Fig. 4b) at 284.6 eV corresponds to the C–C peak, whereas the peak at 284 eV corresponds to the sp^2 hybridized carbon atoms (C=C) from graphene.[43] The C=C bond of the sp^2 structure contributes to the high electrical conductivity of graphene nanosheets. The Ni 2p (Fig. 4c) peaks at 855.6 eV and 873.1 eV correspond to Ni $2p_{3/2}$ and Ni $2p_{1/2}$, representing the characteristics of Ni^{2+} for NiSe.[44] The Se 3d (Fig. 4d) peaks at 54.9 and 58.8 eV are ascribed to Se $3d_{5/2}$ and Se $3d_{3/2}$, representing the metal–selenide bond (Ni–Se bonds of NiSe).[45] It reveals that the NiSe–G nanohybrids mainly contain C, Ni^{2+}, and Se^{2-}, indicating the *in situ* growth of NiSe nanoparticles onto the graphene nanosheets.

Raman spectra of graphene oxide, NiSe nanoparticles, and NiSe–G nanohybrid are shown in Fig. 5. In the Raman spectrum of graphene oxide, peaks at around 1340 cm^{-1} and 1582 cm^{-1} correspond to the D band and G-band, respect-

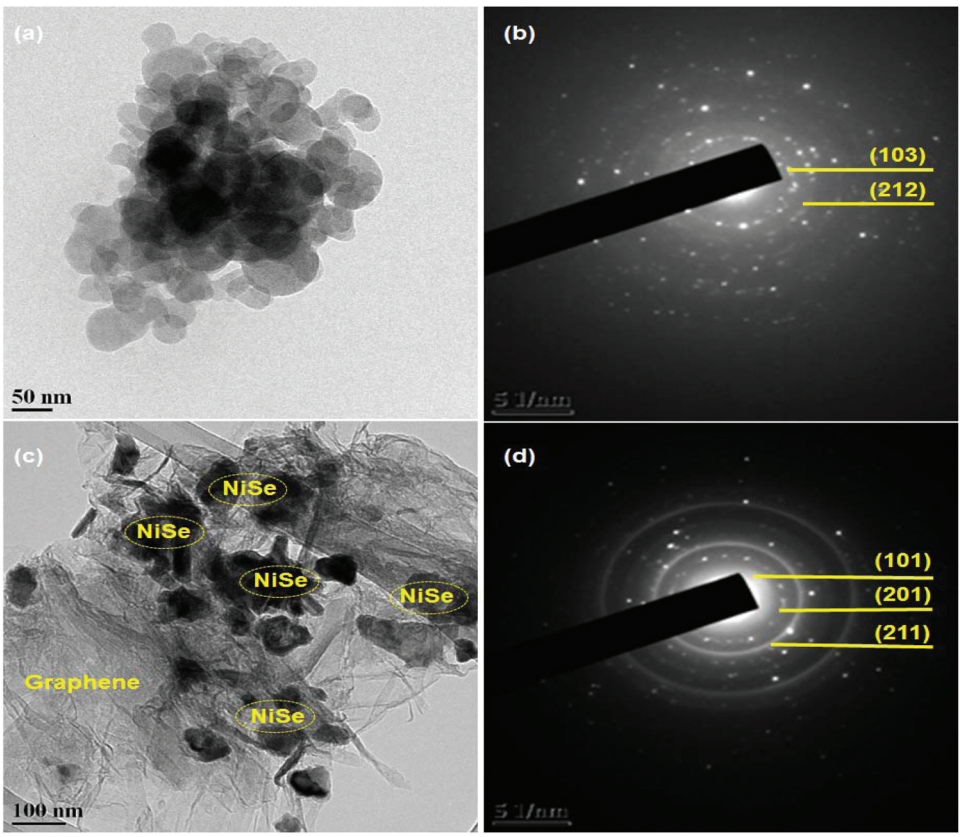

Fig. 2 TEM image of (a) NiSe nanoparticles, (b) SAED patterns of NiSe nanoparticles, (c) NiSe–G nanohybrids, and (d) SAED patterns of NiSe–G nanohybrids.

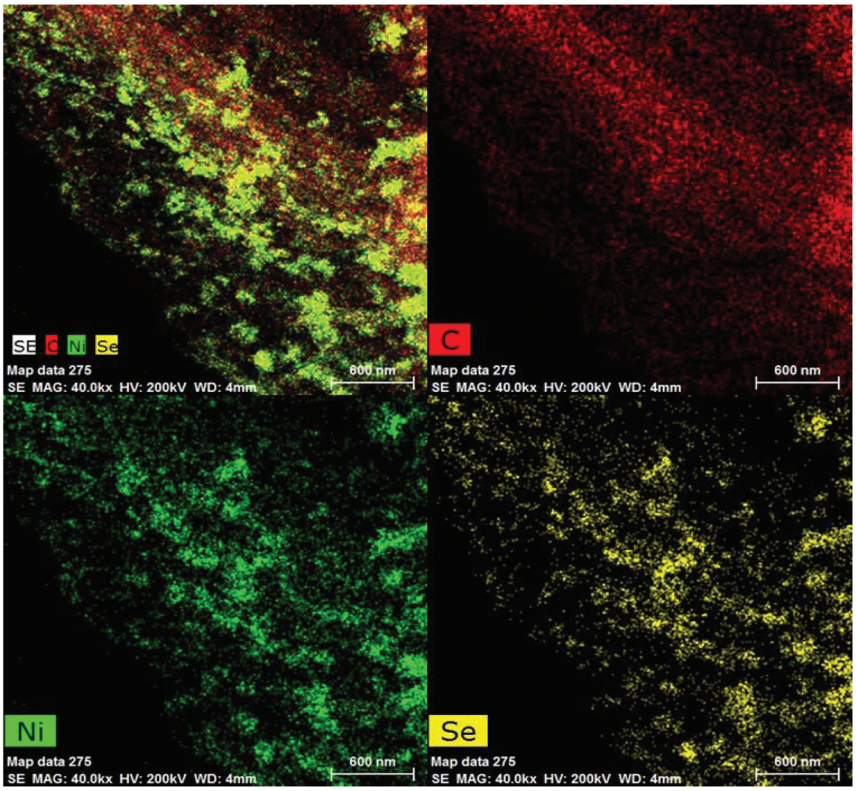

Fig. 3 EDS elemental mapping of C, Ni, and Se elements for NiSe–G nanohybrids by TEM.

ively.[43] The I_D/I_G ratio was found to be 0.71. In the Raman spectrum of NiSe, the peak observed at around 204 cm^{-1} corresponds to the stretching vibration and libration modes or the combination of both the Se–Se pairs (A_g and T_g).[44] The peak at around 506 cm^{-1} can be assigned to the longitudinal optical (LO) one phonon mode of NiSe. There is no indication of elemental selenium, as no peaks were observed at 141 and 235 cm^{-1}.[46] In the Raman spectrum of NiSe–G nanohybrids, a D band at around 1333 cm^{-1} and a G band at around 1582 cm^{-1} are observed. The slight shift of the D band towards the higher frequency region is attributed to the increase in the structural disorder of graphene in NiSe–G.[47] The I_D/I_G ratio for NiSe–G is 1.16. The higher I_D/I_G ratio of NiSe–G nanohybrids than that of graphene oxide is due to the removal of oxygen functional groups in graphene oxide sheets and the re-establishment of numerous small conjugated G-networks (sp^2 domains). This shows that the reduction of graphene oxide and the NiSe Raman modes are suppressed due to the higher intensity of D and G bands of graphene. The inset shows an enlarged version of NiSe–G at particular Raman shifts from 150 to 800 cm^{-1}. It is observed that there is no change in the vibrational mode of NiSe in the NiSe–G nanohybrid. This indicates that there is no phase change in the NiSe nanoparticles due to the addition of graphene.

Fig. 6 shows the X-ray diffraction (XRD) patterns of pure NiSe nanoparticles and NiSe–G nanohybrids. The major diffraction peaks displayed in the XRD pattern of both the samples could be well indexed to the hexagonal phase of $Ni_{0.85}Se$ (JCPDS no. 18-0888) with the lattice constants a = 3.6240 Å, b = 3.6240 Å, and c = 5.2880 Å.[30,48] In the XRD pattern of NiSe–G nanohybrids, the peaks at around 21° and 42.6° correspond to the (002) and (101) planes of graphene nanosheets. Strong and sharp peaks indicate that the active NiSe nanoparticles are well crystallized in the NiSe–G nanohybrid and are also present in adequate quantity. No other impurity peaks appear in the XRD pattern, which indicates that pure NiSe nanoparticles and NiSe–G nanohybrids were formed with high phase purity and crystallinity by a simple hydrothermal method. The diffraction peaks corresponding to nickel selenide nanoparticles in NiSe–G nanohybrids are slightly broader than those of pure NiSe. This indicates that the NiSe nanoparticles on graphene are smaller (~19 nm) in size than pure NiSe (~21 nm) nanoparticles.

The electrochemical performances of single electrode NiSe and NiSe–G are observed through cyclic voltammetry, galvanostatic charge–discharge and electrochemical impedance studies using 6 M KOH as the electrolyte. Fig. 7a shows the CV curve of NiSe and NiSe–G electrodes at a scan rate of 10 mV s^{-1}, with a similar mass loading, and the peak current density of NiSe–G nanohybrids is larger than that of pristine NiSe. This ensures the large amount of charge storage and higher specific capacitance of the NiSe–G nanohybrid electrode. Furthermore, a negligible shift is observed for the reduction potential peak and a very slight shift is observed for the oxidation potential peak of the NiSe–G nanohybrid electrode, as

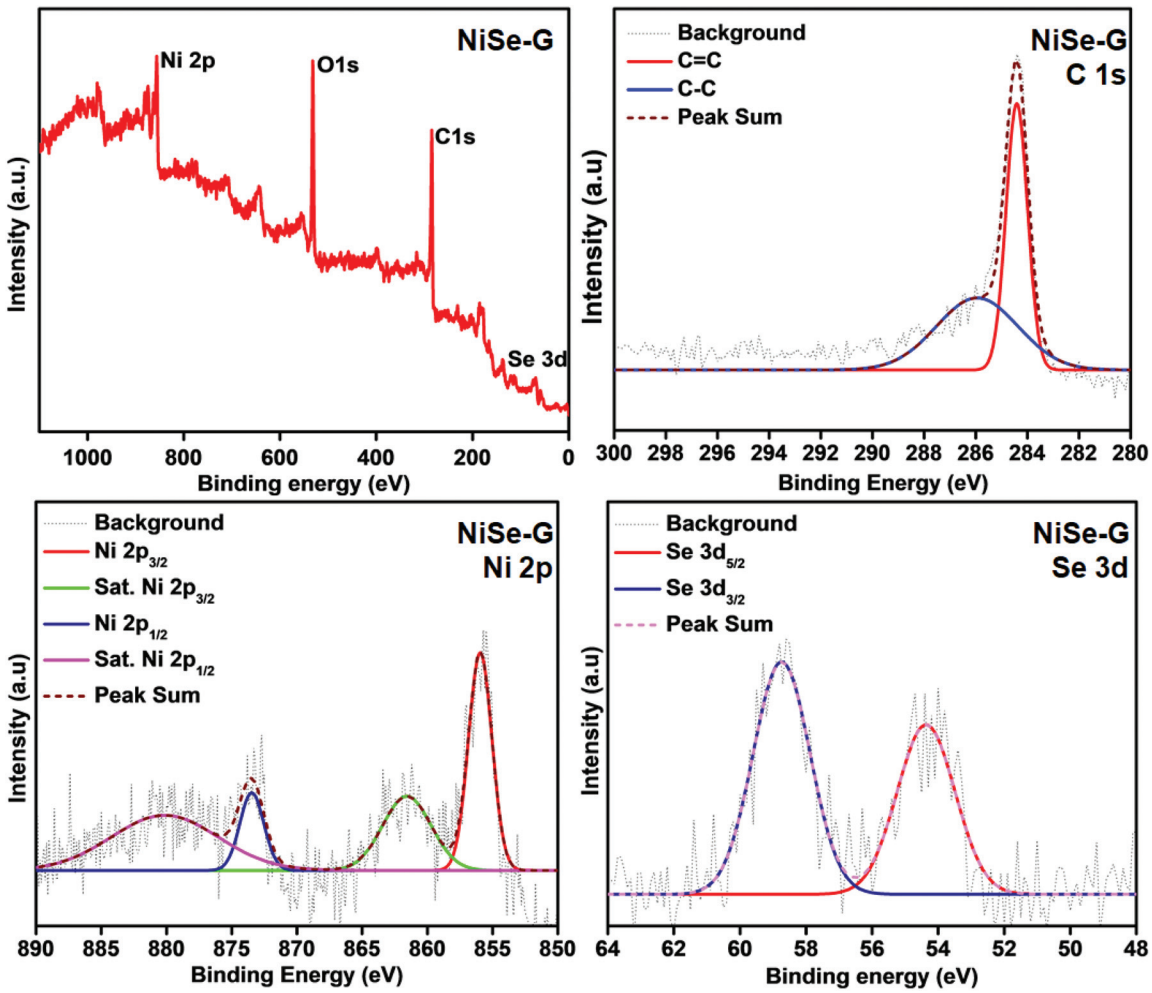

Fig. 4 (a) XPS spectrum of NiSe–G nanohybrids, (b) XPS spectrum of C 1s, (c) XPS spectrum of Ni 2p, and (d) XPS spectrum of Se 3d in NiSe–G nanohybrids.

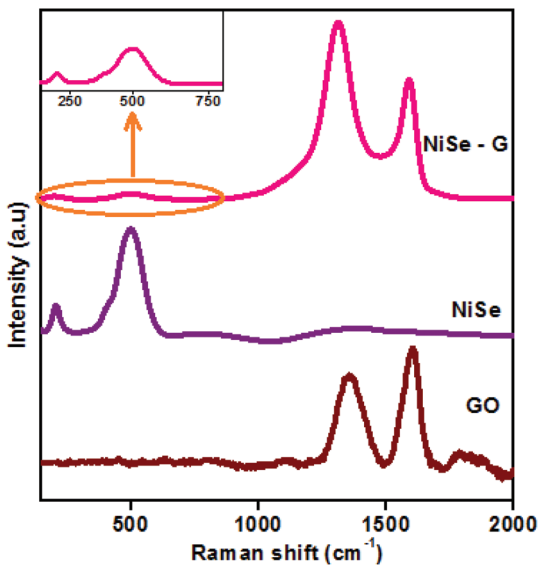

Fig. 5 Raman spectra of GO, NiSe nanoparticles, and NiSe–G nanohybrids.

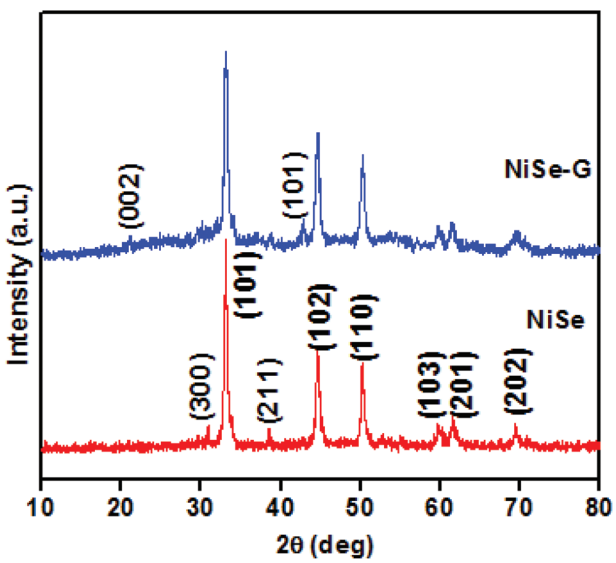

Fig. 6 XRD patterns of NiSe nanoparticles and NiSe–G nanohybrids.

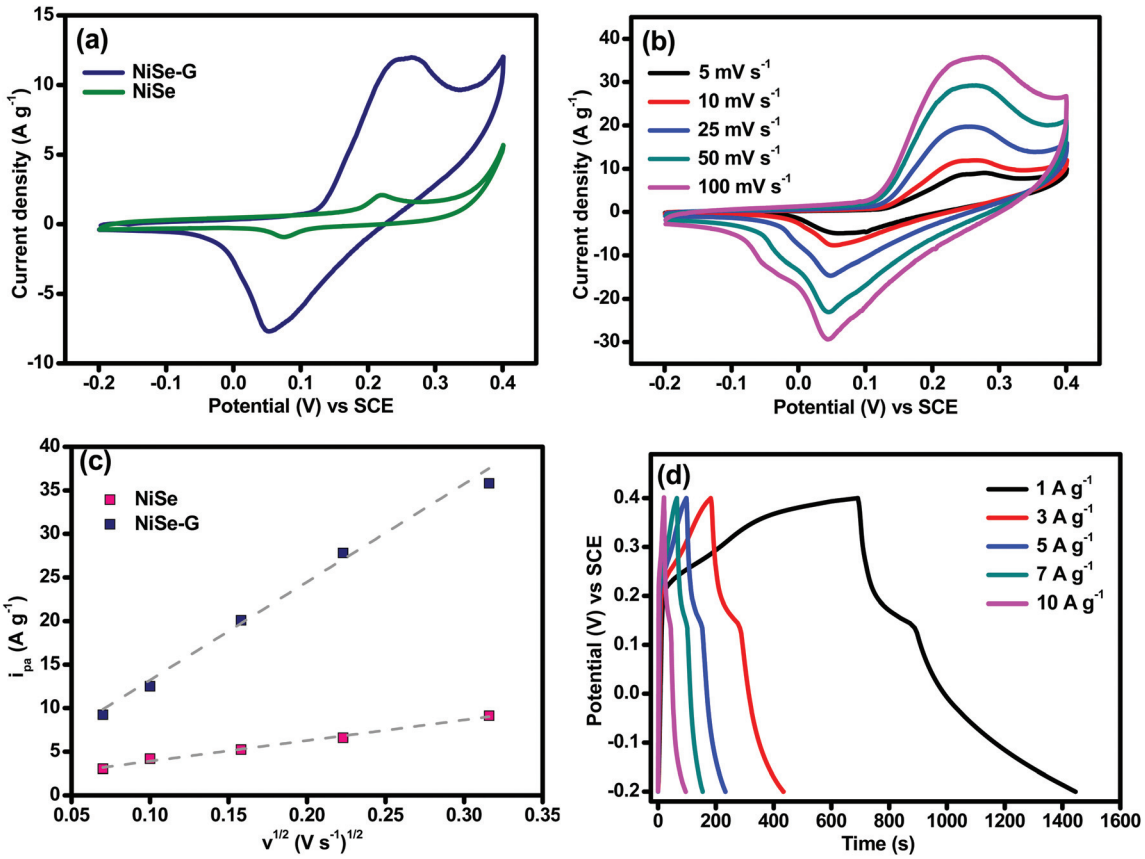

Fig. 7 (a) CV curve of the NiSe and NiSe–G electrode at the scan rate of 10 mV s^{-1}, (b) CV curve of the NiSe–G nanohybrid electrode at various scan rates (5 to 100 mV s^{-1}) in the potential window of −0.2 to +0.4 V *vs.* SCE, (c) relationship between the square root of the scan rate and the anodic peak current of NiSe and the NiSe–G nanohybrid electrode, (d) galvanostatic charge–discharge curves of the NiSe–G nanohybrid electrode at various current densities (1 to 10 A g^{-1}).

compared with the pristine NiSe electrode. This shift is mainly due to the lower internal resistance of the NiSe–G nanohybrid electrode compared with the pristine NiSe electrode, resulting in a better reversible redox reaction. For the NiSe electrode a significant polarization at high potential (0.4 V) is observed, whereas there is no polarization effect in the NiSe–G nanohybrid electrode. The CV curves of NiSe and NiSe–G electrodes are measured in the potential range of −0.2 to +0.4 V (*vs.* SCE) at various scan rates (5–100 mV s^{-1}), see Fig. S3† and 7b, respectively. The CV curve of NiSe (Fig. S3†) exhibits two strong anodic and cathodic peaks at 0.21 V (*vs.* SCE) and 0.07 V (*vs.* SCE) at a scan rate of 5 mV s^{-1}, indicating the oxidation and reduction processes of nickel ions [Ni(II) ↔ Ni(III)]. The NiSe electrode presents a pseudocapacitve nature and the charge storage mechanism is purely a faradaic redox reaction and its proposed reaction mechanism is as follows:[49]

$$\mathrm{NiSe} + \mathrm{OH}^- \rightarrow \mathrm{NiSeOH} + \mathrm{e}^-.$$

The CV curves of NiSe display a symmetrical redox peak at all the scan rates, indicating the high reversibility of the electrode. The CV curve of NiSe–G (Fig. 7b) also exhibits two strong anodic and cathodic peaks at 0.25 V (*vs.* SCE) and 0.06 V (*vs.* SCE) at a scan rate of 5 mV s^{-1}, attributed to the oxidation and reduction process of nickel ions [Ni(II) ↔ Ni(III)].[50] The anodic and cathodic peaks of the NiSe–G nanohybrid electrode are shifted slightly to the right and the left, indicating that the kinetics of the electrode mainly depends on the rate-controlling process.[51] Moreover, the area under the CV curves of NiSe–G is more than that of NiSe, suggesting a greater amount of charge storage. This is because the presence of graphene nanosheets improved the adsorption of ions (OH^-) at the interface and creates an electrical double layer. The charge storage process of NiSe–G electrode presents both the mechanisms *i.e.* pseudocapacitance behavior from NiSe and electrical double layer behavior from graphene nanosheets. The peak current density and integral area of the CV curves obviously increase with increasing the scan rate and the redox peaks are clearly visualized even at a higher scan rate of 100 mV s^{-1}. This reveals that the NiSe–G electrode has a higher rate capability and a more reversible nature in the KOH electrolyte. Fig. 7c presents a relationship between the square root of the scan rate $(\nu)^{1/2}$ and the anodic peak current (i_{pa}). Both NiSe and NiSe–G electrodes show a linear behavior between $\nu^{1/2}$ and i_{pa}, which indicates that the redox reaction mainly depends on the diffusion controlled process.[52,53]

The galvanostatic charge–discharge (GCD) processes for NiSe and NiSe–G electrodes were performed to determine the capacitive performance, specific capacitance, and rate capability. The galvanostatic charge–discharge curves of NiSe and NiSe–G electrodes are tested in the potential range of −0.2 V to +0.4 V (*vs.* SCE) at various current densities from 1 to 10 A g^{-1}, see Fig. S4† and 7d. Both the GCD curves have plateaus, which further confirms the anodic and cathodic peaks in the CV curves, indicating the pseudocapacitive nature of the electrodes. The NiSe discharge curve (Fig. S4†) consists of one sluggish potential drop favoring the redox reaction of nickel ions and another potential drop that indicates the internal resistance of the electrode.[54] But, in the case of the NiSe–G discharge curve (Fig. 7d), two sluggish potential drops are observed; one denotes the redox reaction of nickel ions and another is attributed to the slow adsorption/desorption of OH^- ions onto the graphene sheets associated with redox reaction of Ni^{2+}/Ni^{3+}.[55,56] The nonlinear discharge curve of the NiSe–G electrode takes more time to discharge than NiSe. Obviously, the specific capacitance of NiSe–G is higher than that of NiSe. The calculated specific capacitance of both the electrodes from eqn (1) was found to be 1280, 1232, 1133, 1073 and 1026 F g^{-1} for the NiSe–G electrode and 705, 650, 633, 571 and 483 F g^{-1} for the NiSe electrode at a current density of 1, 3, 5, 7 and 10 A g^{-1}, respectively, see Fig. S5.† Increasing the current density leads to an increase in the voltage drop with lower redox reaction, which significantly reduces the specific capacitance. The NiSe–G electrode has maintained a specific capacitance of 1026 F g^{-1} even at a higher current density (for example, 10 A g^{-1}), manifesting an excellent rate capability of 80%; however, only 69% is maintained under a higher current density for the NiSe electrode. A low coulombic efficiency is observed from the GCD curve of the NiSe electrode due to polarization at the higher voltage (0.4 V), whereas the NiSe–G nanohybrid electrode exhibiting a higher coulombic efficiency with no IR drop in the discharge curves, demonstrates a minimum internal resistance with a better contact between the electrode and the substrate material.

The electrochemical impedance analysis was conducted to determine the resistivity, charge-transfer characteristic and ion diffusion behavior of the NiSe and NiSe–G electrodes. Fig. 8a shows the Nyquist plots of both the NiSe and NiSe–G electrodes, showing a quasi-semicircle followed by a straight line. In general, the quasi-semicircle in the higher frequency region corresponds to the interfacial charge transfer resistance, while the straight line in the lower frequency region corresponds to the Warburg impedance that indicates the electrolyte ions' diffusion in the electrode.[57] In the high frequency region, the NiSe electrode shows a quasi-semicircle whereas the NiSe–G electrode shows negligible semi-circular shapes indicating that both the electrodes possess a low interfacial charge-transfer resistance (R_{ct}).[58] In the lower frequency region, a straight line towards the $-Z''$ axis is observed for the NiSe–G electrode, whereas an inclined line is observed for the NiSe electrode. The NiSe–G electrode favors an ideal capacitive behavior with lower diffusion resistance.[59] The inset in Fig. 8a shows the equivalent circuit fitted for the resulting electrochemical impedance data, where R_s denotes bulk solution resistance, R_{ct} represents charge-transfer resistance, CPE accounts for constant phase elements due to double-layer capacitance, Z_w indicates the Warburg diffusion resistance, and C_f represents faradaic pseudocapacitive element. In the higher frequency region, the intercept on the Z′ axis is the equivalent series resistance (ESR) that gives information about the internal resistance of the electrode, contact resistance between the electrodes and current collectors and the ohmic resistance of the electrolyte. The R_s value of NiSe–G is found to be 0.11 Ω, lower than that of NiSe (0.73 Ω), implying a lower ESR with a better electrical conductivity. The R_{ct} of NiSe–G is 0.77 Ω and that for NiSe is found to be 1.17 Ω. The NiSe–G electrode possesses a lower ESR and R_{ct} values along with the ideal vertical line, suggesting good electrochemical conductivity, enhanced ion diffusion rate and ideal capacitive behavior.[53] The cyclic stability of NiSe and NiSe–G electrodes studied over 2500 charge–discharge cycles at a current density of 5 A g^{-1} is displayed in Fig. 8b.

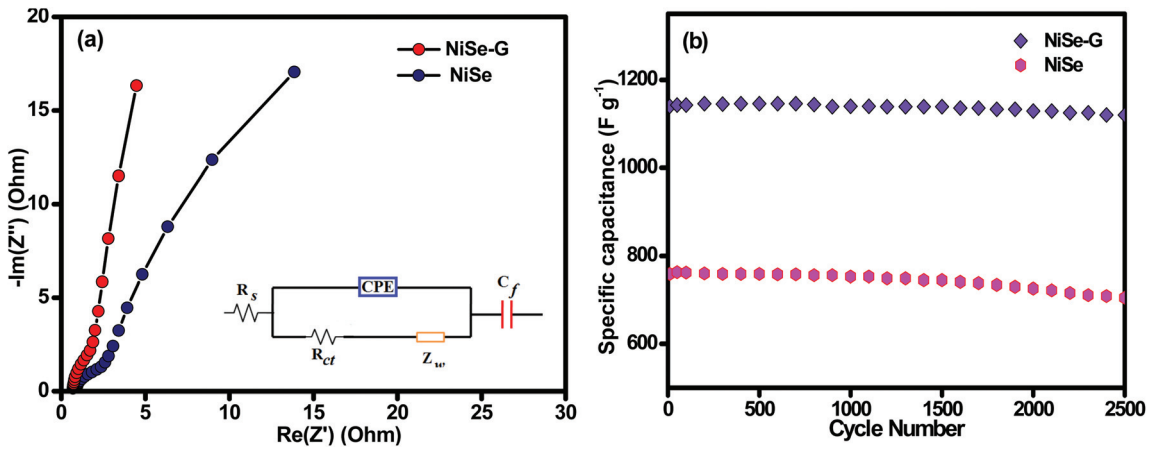

Fig. 8 (a) Nyquist plots of NiSe and NiSe–G (inset: the equivalent circuit), and (b) cyclic stability of NiSe and NiSe–G electrodes at a constant current density of 5 A g^{-1}.

After 2500 cycles, the NiSe–G electrode exhibits 98% capacitance retention, whereas NiSe retained only 92% of its initial capacitance. Interestingly, NiSe–G exhibits a higher capacitance retention than NiSe, due to the synergistic effect of graphene nanosheets and NiSe. The NiSe–G electrode exhibits an excellent capacitive performance that may be attributed to the following reasons: (1) the NiSe nanoparticles strongly anchored on the 2D-graphene nanosheets provide a more electroactive area for the redox reaction with better utilization of OH^- ions. (2) The 2D graphene provides a more specific surface area for the electrolytic ions with a shorter ion diffusion pathway and facilitates faster electron transport towards the collector, which significantly reduces the resistance and improves the structural stability of the electrode

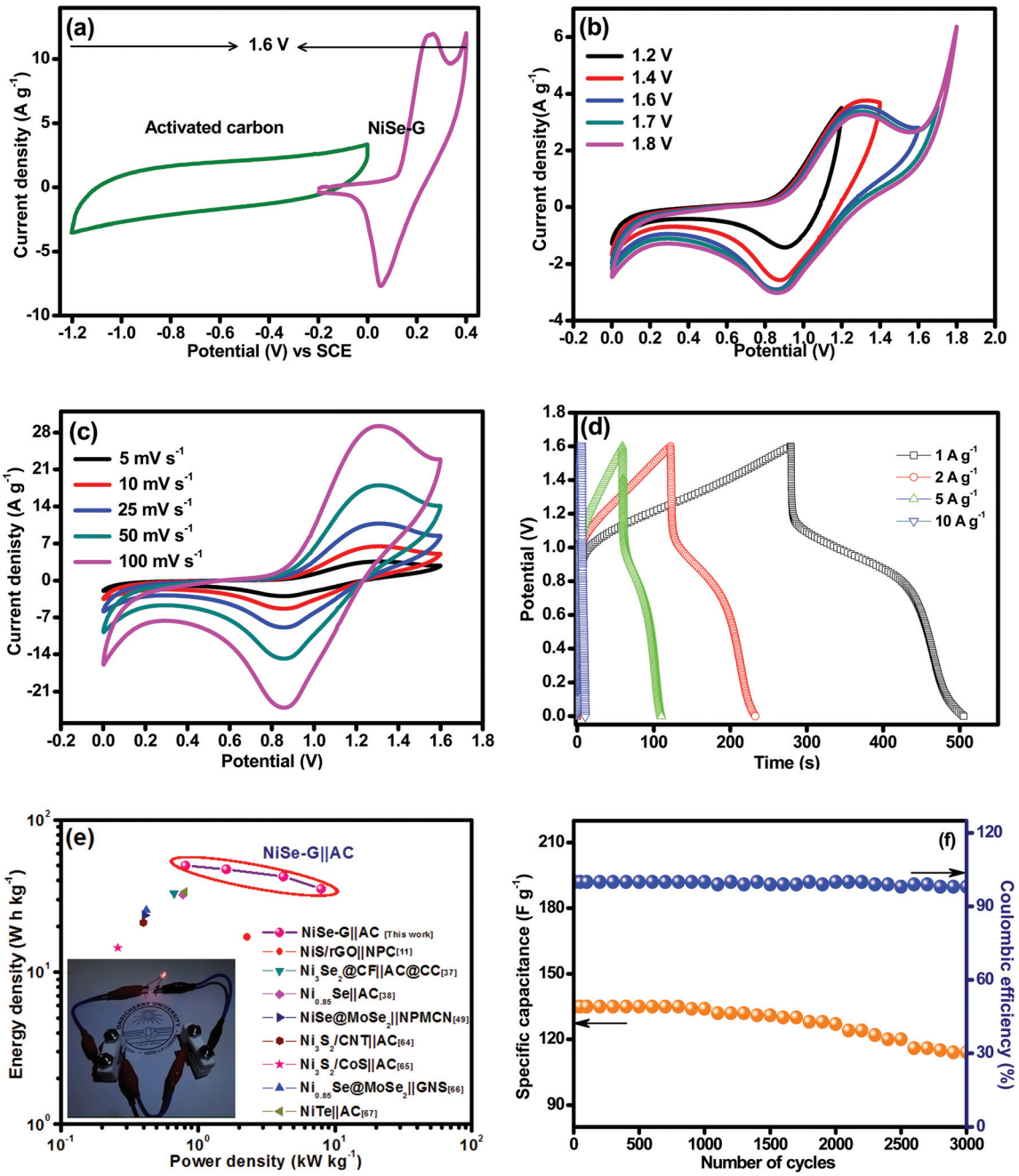

Fig. 9 Electrochemical performance of the NiSe–G||AC ASC device: (a) CV curves of NiSe–G and AC electrodes at a scan rate of 10 mV s^{-1}, (b) CV curves in various voltage windows at a scan rate of 25 mV s^{-1}, (c) CV curves at various scan rates ranging from 5 mV s^{-1} to 100 mV s^{-1}, (d) galvanostatic charge–discharge profile at various current densities from 1 A g^{-1} to 10 A g^{-1}, (e) Ragone plot of the ASC device (inset: two ASC devices connected in series to light up the commercial red LED) (AC – activated carbon, rGO – reduced graphene oxide, NP – nanoporous carbon, CF – conductive fabric, and CC – carbon cloth), and (f) cycling stability test and coulombic efficiency of the ASC device up to 3000 cycles.

material.[60] (3) Metal selenides with alkaline electrolyte exhibit a highly reversible redox reaction and promote more charge storage. For these reasons, NiSe–G can be used as a promising electrode material for supercapacitor application.

For the practical applications of NiSe–G, electrochemical studies are carried out for an asymmetric supercapacitor device, NiSe–G||AC. To determine the potential window of the ASC device, CV measurements for these two electrodes at the scan rate of 10 mV s^{-1} under the three electrode system were carried out, Fig. 9a. The CV curves of NiSe–G and the AC electrodes are −0.2 to +0.4 (*vs.* SCE) and −1.2 to 0.0 V (*vs.* SCE), respectively. The common measured potential range for both the electrodes is 0.0 to −0.2 V and hence a slight overlapping of these two CV curves appears. To obtain an efficient and stable ASC device, the optimum loading mass ratio of NiSe–G to AC should be 0.3, as calculated from eqn (2). Fig. 9b shows the CV curves of the optimized NiSe–G||AC ASC device at various potential windows from 1.2 V to 1.8 V at a scan rate of 10 mV s^{-1}. Actually, no peak is observed up to 1.4 V. But, at 1.6 V, the anodic and cathodic peaks are observed. By increasing the operating voltage up to 1.7 V the CV curve still maintained the redox reaction well with no water splitting, but the charge time of the ASC device is significantly greater than the discharge time at low current density (1 A g^{-1}), which leads to poor coulombic efficiency (Fig. S6†); whereas, in the high potential window of 1.8 V, the CV curve exhibits a sharp current density indicating the evolution of hydrogen that leads to damage of the electrodes. Thus the NiSe–G||AC ASC device can be operated at the potential window of up to 1.6 V for stable electrochemical performance.

Fig. 9c shows the CV curves of NiSe–G||AC at different scan rates ranging from 5 to 100 mV s^{-1} in the potential window of 0.0 to 1.6 V. The charge storage mechanism of the ASC device indicates both pseudocapacitance and electrical double layer capacitance contributions. The shape of the CV curve exhibits a redox peak from the positive electrode (NiSe–G) and there is no obvious distortion observed even at higher scan rate, which implies good reversibility of the ASC device. Fig. 9d demonstrates the galvanostatic charge–discharge (GCD) of NiSe–G||AC at different current densities ranging from 1 to 10 A g^{-1} in the potential window of 0.0 to 1.6 V. The plateaus in the discharge curve are well consistent with CV curves, which is due to the redox reaction of nickel selenide, and the slanted line indicates the surface adsorption and desorption of ions. From the GDC curves using eqn (1), the calculated specific capacitance for the NiSe–G||AC ASC device is found to be 141, 135, 128 and 99 F g^{-1} at a current density of 1, 2, 5 and 10 A g^{-1}, respectively. Thus, the fabricated ASC device shows better rate capability with 70% of capacitance retention at a high current density of 10 A g^{-1}. The energy and power densities of the NiSe–G||AC ASC device were calculated using eqn (3) and (4) and are shown in Fig. 9e. The maximum energy density is 50.1 W h kg^{-1} at a power density of 816 W kg^{-1}; even at a higher current density of 10 A g^{-1}, the ASC device reaches a higher energy density of 35.2 W h kg^{-1} at a power density of 7.92 kW kg^{-1}, which is significantly superior to most of the previously reported chalcogenides and its composites as the positive electrode for the ASC (Table 1).

To determine the viability of the fabricated ASC device, two ASC devices were assembled in series to light a commercial red light emitting diode (LED 2.0 V). Two ASC devices are charged for 5 s to deliver a power output of 3.2 V and easily lighted the red LED (inset in Fig. 9e). The cyclic stability is performed at a constant current density of 1 A g^{-1} for 3000 continuous charge–discharge cycles between 0 and 1.6 V (Fig. 9f). The NiSe–G||AC ASC device maintained a better cycling stability with a capacitance retention of 84.4% even after 3000 cycles with 98% of coulombic efficiency. This is attributed to the excellent reversible redox reaction between the electrode and the electrolyte that provides better electrochemical stability.

Table 1 Summary of the so far reported ASC devices based on chalcogenides and their composites as positive electrodes

Cell configuration	Electrolyte	Cell voltage (V)	CD (A g^{-1})	C_{sp} (F g^{-1})	ED (W h kg^{-1})	PD (kW kg^{-1})	Ref.
NiS/rGO‖NPC	3 M KOH	1.6	2.0	47.8	17.0	2.28	11
CoSe-G‖AC	6 M KOH	1.6	1.0	128.0	45.5	1.10	28
Ni_3Se_2NSs@CF‖AC@CC	1 M KOH	1.5	1.0	86.6	32.8	0.67	37
$Ni_{0.85}Se$‖AC	3 M KOH	1.6	1.0	92.9	32.2	0.78	38
3D-CoS/graphene‖AC	2 M KOH	1.6	1.0	80.0	29.0	0.80	58
$Co_{0.85}Se$‖AC	3 M KOH	1.6	1.0	126.0	45.0	0.80	61
$Co_{0.85}Se$‖N-PCNs	2 M KOH	1.6	—	—	21.1	0.40	62
Mo_9Se_{11}‖AC	3 M LiOH	1.6	1.0	55.0	42.0	0.96	63
Ni_3S_2/CNT‖AC	2 M KOH	1.6	1.0	55.8	19.8	0.78	64
Ni_3S_2/CoS‖AC	2 M KOH	1.6	1.4[a]	79.4	14.4	0.26	65
$Ni_{0.85}Se$@$MoSe_2$‖GNS	2 M KOH	1.6	0.5	71.5	25.5	0.42	66
NiSe@MoSe‖NPMCN	2 M KOH	1.6	0.5	91.7	32.6	0.41	49
NiTe‖AC	3 M KOH	1.6	1.0	47.8	33.6	0.80	67
NiSe–G‖AC	**6 M KOH**	**1.6**	**1.0**	**141.0**	**50.1**	**0.81**	**This work**

[a] Current density in mA cm^{-2}. Abbreviations: CD: current density, C_{sp}: specific capacitance, ED: energy density, PD: power density, AC: activated carbon, PNS/rGO-40: nanoporous nickel sulphide-reduced graphene oxide, NC: zeolitic imidazolate framework (ZIF-8) derived nanoporous carbon, N-PCNs: nitrogen-doped porous carbon networks, CoSe-G: cobalt selenide–graphene nanohybrid, Ni_3Se_2 NSs@CF: conductive fabric (CF)-supported cauliflower-like nickel selenide nanostructures, CC: carbon cloth, GNS: graphene nanosheets, NPMCN: nitrogen-doped pomelo mesocarp-based carbon nanosheets.

4. Conclusion

In summary, NiSe–G nanohybrids have been successfully synthesized through an *in situ* hydrothermal approach and have been used as the positive electrode for asymmetric supercapacitors. The prepared NiSe–G hybrid electrode has a high specific capacitance (1280 F g^{-1}), a better rate capability and an excellent cycling stability (98% after 2500 cycles) with low charge transfer resistance (0.77 Ω) relative to NiSe nanoparticles. This enhanced electrochemical performance of NiSe–G is mainly due to its synergistic effect. The graphene nanosheets prevent the aggregation of NiSe nanoparticles whereas the NiSe provides more electrochemically active sites that enhance the supercapacitive performance. Furthermore, the fabricated ASC device, NiSe–G||AC, exhibits a high specific energy density of 50.1 W h kg^{-1} at a specific power density of 816 W kg^{-1}, which is significantly much higher than those of recently reported ASC devices based on chalcogenides as positive electrodes. Also, a red LED is lit up with the fabricated ASC device, which is evidence that the device can be used for practical applications.

Conflicts of interest

There are no conflicts to declare.

Acknowledgements

The authors gratefully acknowledge the Central Instrumentation Facility (CIF), Pondicherry University for providing instrument facilities. Mr BK gratefully acknowledges the UGC, New Delhi for providing a fellowship under the NFOBC scheme. Mr MV is grateful to the Indo-US Science and Technology Forum (IUSSTF), Department of Science and Technology (DST), New Delhi for providing a fellowship under the Indo-US BASE program (IUSSTF BASE Internships 2018/12/ Vignesh M, dated 09/04/2018).

References

1 D. P. Dubal, O. Ayyad, V. Ruiz and P. Gomez-Romero, *Chem. Soc. Rev.*, 2015, **44**, 1777–1790.
2 (*a*) X. Wang, X. Zeng and D. Cao, *Eng. Sci.*, 2018, **1**, 55–63; (*b*) S. Chen, W. Xing, J. Duan, X. Hu and S. Z. Qiao, *J. Mater. Chem. A*, 2013, **1**, 2941–2954.
3 (*a*) W. Deng, T. Kang, H. Liu, J. Zhang, N. Wang, N. Lu, Y. Ma, A. Umar and Z. Guo, *Sci. Adv. Mater.*, 2018, **10**, 937–949; (*b*) X. Li, W. Zhao, R. Yin, X. Huang and L. Qian, *Eng. Sci.*, 2018, **3**, 89–95.
4 (*a*) A. K. Solarajan, V. Murugadoss and S. Angaiah, *J. Appl. Polym. Sci.*, 2017, **134**, 45177; (*b*) F. Ran, X. Yang and L. Shao, *Adv. Compos. Hybrid Mater.*, 2018, **1**, 32–55.
5 G. Wang, L. Zhang and J. Zhang, *Chem. Soc. Rev.*, 2012, **41**, 797–828.
6 H. Khani and D. O. Wipf, *ACS Appl. Mater. Interfaces*, 2017, **9**, 6967–6978.
7 C. Lin, L. Hu, C. Cheng, K. Sun, X. Guo, Q. Shao, J. Li, N. Wang and Z. Guo, *Electrochim. Acta*, 2018, **260**, 65–72.
8 S. Vijayan, B. Kirubasankar, P. Pazhamalai, A. K. Solarajan and S. Angaiah, *ChemElectroChem*, 2017, **4**, 2059–2067.
9 B. Liu, D. Kong, Z. X. Huang, R. Mo, Y. Wang, Z. Han, C. Cheng and H. Y. Yang, *Nanoscale*, 2016, **8**, 10686–10694.
10 T. Peng, H. Yi, P. Sun, Y. Jing, R. Wang, H. Wang and X. Wang, *J. Mater. Chem. A*, 2016, **4**, 8888–8897.
11 P. R. Jothi, R. R. Salunkhe, M. Pramanik, S. Kannan and Y. Yamauchi, *RSC Adv.*, 2016, **6**, 21246–21253.
12 X. Lou, C. Lin, Q. Luo, J. Zhao, B. Wang, J. Li, Q. Shao, X. Guo, N. Wang and Z. Guo, *ChemElectroChem*, 2017, **4**, 3171–3180.
13 (*a*) M. Sevilla and R. Mokaya, *Energy Environ. Sci.*, 2014, **7**, 1250–1280; (*b*) S. Zhou, J. Wang, S. Wang, X. Ma, J. Huang, G. Zhao and Y. Liu, *Mater. Chem. Phys.*, 2018, **217**, 315–322; (*c*) L. Qiu, P. Guo, H. Zou, Y. Feng, X. Zhang, S. Pervaiz and D. Wen, *ES Energy Environ.*, 2018, DOI: 10.30919/esee8c139, in press; (*d*) Z. Wang, R. Wei, J. Gu, H. Liu, C. Liu, C. Luo, J. Kong, Q. Shao, N. Wang, Z. Guo and X. Liu, *Carbon*, 2018, **139**, 1126–1135; (*e*) Q. Luo, H. Ma, Q. Hou, Y. Li, J. Ren, X. Dai, Z. Yao, Y. Zhou, L. Xiang, H. Du, H. He, N. Wang, K. Jiang, H. Lin, H. Zhang and Z. Guo, *Adv. Funct. Mater.*, 2018, **28**, 1706777.
14 J. Shen, J. Wu, L. Pei, M.-T. F. Rodrigues, Z. Zhang, F. Zhang, X. Zhang, P. M. Ajayan and M. Ye, *Adv. Energy Mater.*, 2016, **6**, 1600341.
15 J. Yang, C. Yu, X. Fan, S. Liang, S. Li, H. Huang, Z. Ling, C. Hao and J. Qiu, *Energy Environ. Sci.*, 2016, **9**, 1299–1307.
16 X. Xiong, G. Waller, D. Ding, D. Chen, B. Rainwater, B. Zhao, Z. Wang and M. Liu, *Nano Energy*, 2015, **16**, 71–80.
17 H. Wang, H. Feng and J. Li, *Small*, 2014, **10**, 2165–2181.
18 Y. Zhang, L. Qian, W. Zhao, X. Li, X. Huang, X. Mai, Z. Wang, Q. Shao, X. Yan and Z. Guo, *J. Electrochem. Soc.*, 2018, **165**, H510–H516.
19 B. Song, T. Wang, H. Sun, Q. Shao, J. Zhao, K. Song, L. Hao, L. Wang and Z. Guo, *Dalton Trans.*, 2017, **46**, 15769–15777.
20 N. Wu, C. Liu, D. Xu, J. Liu, W. Liu, Q. Shao and Z. Guo, *ACS Sustainable Chem. Eng.*, 2018, **6**, 12471–12480.
21 (*a*) L. Wu, L. Hao, B. Pang, G. Wang, Y. Zhang and X. Li, *J. Mater. Chem. A*, 2017, **5**, 4629–4637; (*b*) X.-C. Zhao, P. Yang, L.-J. Yang, Y. Cheng, H.-Y. Chen, H. Liu, G. Wang, V. Murugadoss, S. Angaiah and Z. Guo, *ES Mater. Manuf.*, 2018, DOI: 10.30919/esmm5f109, in press; (*c*) Y. Feng, E. Witkoske, E. S. Bell, Y. Wang, A. Tzempelikos, I. T. Ferguson and N. Lu, *ES Mater. Manuf.*, 2018, DOI: 10.30919/esmm5f116, in press; (*d*) S. Hu, Z. Zhang, Z. Wang, K. Zeng, Y. Cheng, J. Chen and G. Zhang, *ES Energy Environ.*, 2018, DOI: 10.30919/esee8c140, in press; (*e*) M. Waqas, P. M. Kouotou, A. E. Kasmi, Y. Wang and Z.-Y. Tian, *ES Energy Environ.*, 2018, DOI: 10.30919/esee8c145, in press.
22 L. Shen, L. Yu, H. B. Wu, X.-Y. Yu, X. Zhang and X. W. Lou, *Nat. Commun.*, 2015, **6**, 6694.

23 K.-J. Huang, J.-Z. Zhang and J.-L. Cai, *Electrochim. Acta*, 2015, **180**, 770–777.
24 Q. Hou, J. Ren, H. Chen, P. Yang, Q. Shao, M. Zhao, X. Zhao, H. He, N. Wang, Q. Luo and Z. Guo, *ChemElectroChem*, 2018, **5**, 726–731.
25 T. Lu, S. Dong, C. Zhang, L. Zhang and G. Cui, *Compos. Interfaces*, 2017, **332**, 75–99.
26 S. H. Park, Y.-K. Sun, K. S. Park, K. S. Nahm, Y. S. Lee and M. Yoshio, *Electrochim. Acta*, 2002, **47**, 1721–1726.
27 Z. Zeng, D. Wang, J. Zhu, F. Xiao, Y. Li and X. Zhu, *CrystEngComm*, 2016, **18**, 2363–2374.
28 B. Kirubasankar, V. Murugadoss and S. Angaiah, *RSC Adv.*, 2017, **7**, 5853–5862.
29 (*a*) L. Zhang, M. Qin, W. Yu, Q. Zhang, H. Xie, Z. Sun, Q. Shao, X. Guo, L. Hao, Y. Zheng and Z. Guo, *J. Electrochem. Soc.*, 2017, **164**, H1086–H1090; (*b*) H. Du, C. Zhao, J. Lin, Z. Hu, Q. Shao, J. Guo, B. Wang, D. Pan, E. K. Wujcik and Z. Guo, *Chem. Rec.*, 2018, **18**, 1365–1372; (*c*) C. Wang, B. Mo, Z. He, C. X. Zhao, L. Zhang, Q. Shao, X. Guo, E. Wujcik and Z. Guo, *Polymer*, 2018, **138**, 363–368; (*d*) C. Wang, B. Mo, Z. He, Q. Shao, D. Pan, E. Wujick, J. Guo, X. Xie, X. Xie and Z. Guo, *J. Membr. Sci.*, 2018, **556**, 118–125.
30 L. Mi, H. Sun, Q. Ding, W. Chen, C. Liu, H. Hou, Z. Zheng and C. Shen, *Dalton Trans.*, 2012, **41**, 12595–12600.
31 (*a*) Z. Zhao, R. Guan, J. Zhang, Z. Zhao and P. Bai, *Acta Metall. Sin. (Engl. Lett.)*, 2017, **30**, 66–72; (*b*) J. S. Cho, S. Y. Lee and Y. C. Kang, *Sci. Rep.*, 2016, **6**, 23338.
32 Z. Gao, J. Qi, M. Chen, W. Zhang and R. Cao, *Electrochim. Acta*, 2017, **224**, 412–418.
33 (*a*) X. Zhang, M. Zhen, J. Bai, S. Jin and L. Liu, *ACS Appl. Mater. Interfaces*, 2016, **8**, 17187–17193; (*b*) Z. Zhao, P. Bai1, R. Guan, V. Murugadoss, H. Liu, X. Wang and Z. Guo, *Mater. Sci. Eng., A*, 2018, **734**, 200–209.
34 C. Tang, N. Cheng, Z. Pu, W. Xing and X. Sun, *Angew. Chem., Int. Ed.*, 2015, **54**, 9351–9355.
35 T. Su, Q. Shao, Z. Qin, Z. Guo and Z. Wu, *ACS Catal.*, 2018, **8**, 2253–2276.
36 L. Zhang, W. Yu, C. Han, J. Guo, Q. Zhang, H. Xie, Q. Shao, Z. Sun and Z. Guo, *J. Electrochem. Soc.*, 2017, **164**, H651–H656.
37 G. Nagaraju, S. M. Cha, S. C. Sekhar and J. S. Yu, *Adv. Energy Mater.*, 2017, **7**, 1601362.
38 C. Gong, M. Huang, J. Zhang, M. Lai, L. Fan, J. Lin and J. Wu, *RSC Adv.*, 2015, **5**, 81474–81481.
39 X. Sun, Z. Liu, K. Welsher, J. T. Robinson, A. Goodwin, S. Zaric and H. Dai, *Nano Res.*, 2008, **1**, 203–212.
40 A. Solarajan, V. Murugadoss and S. Angaiah, *Appl. Mater. Today*, 2016, **5**, 33–40.
41 M. Kumar, A. Subramania and K. Balakrishnan, *Electrochim. Acta*, 2014, **149**, 152–158.
42 C. Wang, V. Murugadoss, J. Kong, Z. He, X. Mai, Q. Shao, Y. Chen, L. Guo, C. Liu, S. Angaiah and Z. Guo, *Carbon*, 2018, **140**, 696–733.
43 (*a*) V. Murugadoss, N. Wang, S. Tadakamalla, B. Wang, Z. Guo and S. Angaiah, *J. Mater. Chem. A*, 2017, **5**, 14583–14594; (*b*) H. Liu, M. Dong, W. Huang, J. Gao, K. Dai, J. Guo, G. Zheng, C. Liu, C. Shen and Z. Guo, *J. Mater. Chem. C*, 2017, **5**, 73–83; (*c*) T. Liu, K. Yu, L. Gao, H. Chen, N. Wang, L. Hao, T. Li, H. He and Z. Guo, *J. Mater. Chem. A*, 2017, **5**, 17848–17855.
44 W. Shi, X. Zhang and G. Che, *Int. J. Hydrogen Energy*, 2013, **38**, 7037–7045.
45 H. Chen, S. Chen, M. Fan, C. Li, D. Chen, G. Tian and K. Shu, *J. Mater. Chem. A*, 2015, **3**, 23653–23659.
46 A. T. Swesi, J. Masud and M. Nath, *Energy Environ. Sci.*, 2016, **9**, 1771–1782.
47 R. P. Vidano, D. B. Fischbach, L. J. Willis and T. M. Loehr, *Solid State Commun.*, 1981, **39**, 341–344.
48 B. Yuan, W. Luan and S.-T. Tu, *CrystEngComm*, 2012, **14**, 2145–2151.
49 H. Peng, J. Zhou, K. Sun, G. Ma, Z. Zhang, E. Feng and Z. Lei, *ACS Sustainable Chem. Eng.*, 2017, **5**, 5951–5963.
50 H. Yi, H. Wang, Y. Jing, T. Peng, Y. Wang, J. Guo, Q. He, Z. Guo and X. Wang, *J. Mater. Chem. A*, 2015, **3**, 19545–19555.
51 J. Kang, A. Hirata, H.-J. Qiu, L. Chen, X. Ge, T. Fujita and M. Chen, *Adv. Mater.*, 2014, **26**, 269–272.
52 W. Sun, X. Rui, M. Ulaganathan, S. Madhavi and Q. Yan, *J. Power Sources*, 2015, **295**, 323–328.
53 C. Zhang, Q. Chen and H. Zhan, *ACS Appl. Mater. Interfaces*, 2016, **8**, 22977–22987.
54 X. Wang, X. Li, X. Du, X. Ma, X. Hao, C. Xue, H. Zhu and S. Li, *Electroanalysis*, 2017, **29**, 1286–1293.
55 H. Wang, Z. Xu, H. Yi, H. Wei, Z. Guo and X. Wang, *Nano Energy*, 2014, **7**, 86–96.
56 W. Zhou, D. Kong, X. Jia, C. Ding, C. Cheng and G. Wen, *J. Mater. Chem. A*, 2014, **2**, 6310–6315.
57 H. Xie, S. Tang, D. Li, S. Vongehr and X. Meng, *ChemSusChem*, 2017, **10**, 2301–2308.
58 J. Shi, X. Li, G. He, L. Zhang and M. Li, *J. Mater. Chem. A*, 2015, **3**, 20619–20626.
59 B. Mu, W. Zhang, S. Shao and A. Wang, *Phys. Chem. Chem. Phys.*, 2014, **16**, 7872–7880.
60 Z. Yang, X. Hao, S. Chen, Z. Ma, W. Wang, C. Wang, L. Yue, H. Sun, Q. Shao, V. Murugadoss and Z. Guo, *J. Colloid Interface Sci.*, 2019, **533**, 13–23.
61 J. Yang, Y. Yuan, W. Wang, H. Tang, Z. Ye and J. Lu, *J. Power Sources*, 2017, **340**, 6–13.
62 H. Peng, G. Ma, K. Sun, Z. Zhang, J. Li, X. Zhou and Z. Lei, *J. Power Sources*, 2015, **297**, 351–358.
63 R. A. Aziz, S. K. Muzakir, I. I. Misnon, J. Ismail and R. Jose, *J. Alloys Compd.*, 2016, **673**, 390–398.
64 C.-S. Dai, P.-Y. Chien, J.-Y. Lin, S.-W. Chou, W.-K. Wu, P.-H. Li, K.-Y. Wu and T.-W. Lin, *ACS Appl. Mater. Interfaces*, 2013, **5**, 12168–12174.
65 R. Li, S. Wang, J. Wang and Z. Huang, *Phys. Chem. Chem. Phys.*, 2015, **17**, 16434–16442.
66 H. Peng, C. Wei, K. Wang, T. Meng, G. Ma, Z. Lei and X. Gong, *ACS Appl. Mater. Interfaces*, 2017, **9**, 17067–17075.
67 P. Zhou, L. Fan, J. Wu, C. Gong, J. Zhang and Y. Tu, *J. Alloys Compd.*, 2016, **685**, 384–390.